



Experimental validation of a numerical model for predicting the trajectory of blood drops in typical crime scene conditions, including droplet deformation and breakup, with a study of the effect of indoor air currents and wind on typical spatter drop trajectories

N. Kabaliuk^a, M.C. Jermy^{a,*}, E. Williams^{b,c}, T.L. Laber^d, M.C. Taylor^b

^a Department of Mechanical Engineering, University of Canterbury, Private Bag 4800, Christchurch 8041, New Zealand

^b Christchurch Science Centre, Institute of Environmental Sciences and Research, 27 Croyke Road, Christchurch 8041, New Zealand

^c Department of Sport and Exercise Science, Faculty of Science, University of Auckland, Private Bag 92019, Auckland 1142, New Zealand

^d Minnesota Bureau of Criminal Apprehension, 1430 Maryland Ave. East, St. Paul, MN 55106, United States

ARTICLE INFO

Article history:

Received 17 April 2014

Received in revised form 14 September 2014

Accepted 1 October 2014

Available online 18 October 2014

Keywords:

Bloodstain pattern analysis

Numerical modeling

Droplet breakup

Droplet oscillation

Drag

Trajectory

ABSTRACT

Bloodstain Pattern Analysis (BPA) provides information about events during an assault, e.g. location of participants, weapon type and number of blows. To extract the maximum information from spatter stains, the size, velocity and direction of the drop that produces each stain, and forces acting during flight, must be known.

A numerical scheme for accurate modeling of blood drop flight, in typical crime scene conditions, including droplet oscillation, deformation and in-flight disintegration, was developed and validated against analytical and experimental data including passive blood drop oscillations, deformation at terminal velocity, cast-off and impact drop deformation and breakup features. 4th order Runge–Kutta timestepping was used with the Taylor Analogy Breakup (TAB) model and Pilch and Erdman's (1987) expression for breakup time. Experimental data for terminal velocities, oscillations, and deformation was obtained via digital high-speed imaging. A single model was found to describe drop behavior accurately in passive, cast off and impact scenarios.

Terminal velocities of typical passive drops falling up to 8 m, distances and times required to reach them were predicted within 5%. Initial oscillations of passive blood drops with diameters of $1\text{ mm} < d < 6\text{ mm}$ falling up to 1.5 m were studied. Predictions of oscillating passive drop aspect ratio were within 1.6% of experiment. Under typical crime scene conditions, the velocity of the drop within the first 1.5 m of fall is affected little by drag, oscillation or deformation.

Blood drops with diameter 0.4–4 mm and velocity 1–15 m/s cast-off from a rotating disk showed low deformation levels (Weber number < 3). Drops formed by blunt impact 0.1–2 mm in diameter at velocities of 14–25 m/s were highly deformed (aspect ratios down to 0.4) and the larger impact blood drops (~ 1 –1.5 mm in diameter) broke up at critical Weber numbers of 12–14. Most break-ups occurred within 10–20 cm of the impact point. The model predicted deformation levels of cast-off and impact blood drops within 5% of experiment. Under typical crime scene conditions, few cast-off drops will break up in flight. However some impact-generated drops were seen to break up, some by the vibration, others by bag breakup.

The validated model can be used to gain deep understanding of the processes leading to spatter stains, and can be used to answer questions about proposed scenarios, e.g. how far blood drops may travel, or how stain patterns are affected by winds and draughts.

© 2014 Elsevier Ireland Ltd. All rights reserved.

* Corresponding author. Tel.: +64 3 364 2987; fax: +64 3 364 2078.

E-mail address: mark.jermy@canterbury.ac.nz (M.C. Jermy).

1. Introduction

Violent crimes involving bloodshed may result in the formation of a number of blood drops that move through air and eventually impact onto a surface producing a group of bloodstains (or bloodstain pattern). This is termed blood spatter [2].

It has been shown that stain shape can be correlated with the drop impact angle on a target surface (the Sine law: [3–5]). The ‘sine law’ is routinely used in the analysis of crime scene bloodstain patterns. A number of attempts have been made to correlate stain characteristics (size and morphology) to the volume and impact velocity of the blood drop. These studies have all focused on stains formed as a result of blood dripping from a wound or bloodied object (weapon) under the action of gravity ([6–9]; [63]). These approaches have important limitations: the reproducibility in counting of spines and the limited number (or absence) of spines for low velocity impacts on some surfaces. Interpretation of the stain morphology is sometimes difficult, for example due to impact surface irregularities or porosity. Further research is needed for other types of bloodstains and target surfaces.

A common analysis done at a crime scene is the estimation of the position of the blood source in an impact spatter event. If two or more drop trajectories can be determined, the point at which they intersect is the probable location of the victim at the time the wound was inflicted. To determine the trajectory of an individual drop from analyzing stain characteristics certain assumptions need to be made.

The stringing method [10] assumes the drop trajectory is a straight line. Gravitational and drag forces are assumed to have a negligible effect on the direction of flight while the droplet is airborne. The Backtrak[®] (<http://people.physics.carleton.ca/~carter/>) and Hemospat[®] (<http://hemospat.com/research.php>) software programs are based on the straight line trajectory approximation. Straight line blood drop trajectory approximation also underlies the tangent method [11]. These approaches, however, were shown to produce considerable errors in area of origin determination, unless the trajectories are very short and the velocities relatively high [12–14].

Another method of blood source determination proposed by Podworny and Carter [15] assumes parabolic trajectories of spherical drops. Buck et al. [16] and Buck and Kneubuehl [17] argued that this method is adequate for reconstructive purposes.

To assess the accuracy of trajectory reconstruction methods, it is necessary to have an in-depth understanding of the physics of blood droplet flight and impact. This paper deals with predictions of the flight of droplets, for which the initial conditions are known.

In order to accurately predict the trajectory (flight path) of a blood drop to calculate its origin, the initial state of the drop (size, shape and velocity) must be known and the forces acting during flight should be considered.

Depending on the mechanism of formation, a fluid drop may be non-spherical and experience shape oscillations under the influence of surface tension. Drop oscillations are damped exponentially in time by the drop fluid viscosity [18,19].

As the drop travels through air it experiences inertial, gravitational and aerodynamic drag forces. The latter is proportional to drop projected area (the area facing the incident flow), the drag coefficient and the dynamic pressure exerted by the external fluid (air) flow.

Surface tension forces at the free surface act to minimize the drop's surface energy and shape it into the smallest possible surface area, a sphere. When subject to external fluid flow however, a drop deforms to balance normal and shear stresses on its surface [20]. The level of drop deformation depends on the intensity of the deforming aerodynamic force.

Alteration of drop shape changes its drag properties. Distortion toward an oblate shape increases the projected area and drag coefficient (relative to the case of a spherical drop of the same volume). This may lead to a significant alteration in drop trajectory [21], which is of importance to the point of origin determination.

Under certain critical conditions a drop may reach a severe state of deformation, a so-called ‘liquid disc’. The drop may further deform into a hollow sphere or bag, a hollow sphere with a jet or exhibit more irregular deformation and finally disintegrates (or breaks up) into smaller ‘child’ drops [22,23].

This raises two questions: (i) Under typical crime scene conditions, do the deformation and oscillation of blood drops appreciably affect their trajectory? (ii) Is mid-air breakup into smaller drops possible in typical crime scene conditions?

This paper aims to address these issues by developing and validating a numerical code for accurate and detailed blood drop flight modeling. Special attention is given to blood drops produced as a result of passive dripping, cast-off and impact. The numerical simulation described here provides a reliable and non-laborious method for understanding and predicting the flight characteristics of spatter drops.

2. Mechanisms of spatter drop generation

The external force which causes the victim's blood to break up into airborne drops may be gravity (drip or passive stains), blunt force impact (impact patterns), centripetal acceleration (cast-off) or bullet impact (gunshot spatter patterns).

The characteristics of typical blood drop formation and flight in the fluid dynamics framework are described below. Further discussion of the physics of drop formation is given in Jermy and Taylor [24] and Attinger et al. [25]. Further to the material in those sources, an estimate of the range of drop sizes, velocities and key non-dimensional parameters is given below.

Table 1

Blood drop characteristics in BPA, where $\rho_{\text{air}} = 1.2 \text{ kg/m}^3$, $\nu_{\text{air}} = 1.51 \times 10^{-5} \text{ m}^2/\text{s}$ are air density and kinematic viscosity at 20 °C; $\rho = 1056 \text{ kg/m}^3$, $\mu = 4 \text{ mN s/m}^2$, $\sigma = 56 \text{ mN/m}$ are blood density, high-shear-rate viscosity and surface tension, respectively, at 37 °C.

Mechanism	<i>d</i> , mm	<i>V</i> , m/s	<i>Re</i>	<i>We</i>	<i>We</i> _{avg}	<i>Bo</i>	<i>Oh</i>
Passive dripping [6,55]	3–7	<7	<3200	<7	~1	<9	~0.01
Cast-off [8,11,56]	0.5–4	1.5–20	50–5300	0.02–34	~6	0.05–3	0.01–0.02
Impact [8,56,57]	0.2–2	1.5–30	20–4000	0.01–39	~6	0.01–0.7	0.01–0.04
Gunshot [4,6]	0.05–1 ^a	15–45 ^b	50–2000	0.24–43	~10	<0.2	0.02–0.07

^a Because of the lack of experimental data on gunshot related spatter, the size and velocity of the gunshot-induced drops have been estimated. Drop volume (and hence diameter) was based on the reported gunshot spatter stain sizes (areas) and estimated stain thickness (calculated as a constant, $\sim 10^2$ – 10^3 , times erythrocyte dimensions).

^b In some instances gunshot spatter may be affected by firearm muzzle gases [58]. In this case the relative velocity between the gases in fast movement and the drop should be used for Weber number calculation. This would depend on the proximity to the firearm to the blood source and firearm used. The reported data on the range of magnitudes of relative velocities associated with gunshot is lacking in BPA literature however. To avoid speculation the data from [6] was used instead to provide a reference drop velocity range for gunshot spatter of around 30.5 m/s. The relative velocity may considerably exceed this value.

Passive, cast-off, impact and gunshot-induced drops are characterized in Table 1 according to dimensionless numbers relevant to drop formation and flight:

- Reynolds number ($Re = Vd_o/\nu_{air}$, which is the ratio of inertial to viscous forces acting on a drop),
- Weber number ($We = \rho_{air}V^2d_o/\sigma$, the ratio of inertial and interfacial tension forces),
- Bond number ($Bo = \rho gd_o^2/\sigma$, the ratio of drop weight to interfacial tension forces) and
- Ohnesorge number ($Oh = \mu/\sqrt{\rho d_o \sigma}$, the ratio of viscous to interfacial tension forces).

Where d_o and V are blood drop diameter and velocity; ρ_{air} and μ_{air} are air density and kinematic viscosity; ρ , μ and σ are blood density, viscosity and surface tension, respectively.

The Weber number is as an indicator of the degree of drop deformation [23]. The drop can be considered effectively spherical for $We < 1$, whereas more pronounced deformation is associated with $We > 1-3$ and at We higher than ~ 13 the drop breaks up [26]. The average Weber number, We_{avg} , is based on the average blood drop diameter and velocity.

Fig. 1 shows blood drop sizes and velocities plotted together with the experimental data on terminal velocities of water drops from [27], which were expected to be a good approximation for blood drops at terminal velocity conditions.

Passive drops, the largest of the types considered, rarely reach terminal velocity under crime scene conditions¹ (such as a living room, for example) (see Fig. 1) and, consequently, experience lower levels of aerodynamic deforming force and thus deform to a lesser extent during flight. These, in addition, are prone to high-amplitude initial oscillations [18].

Cast-off and impact drops may begin their flight with velocities much greater than their terminal velocities and possess high levels of deformation (as indicated by $We > 3$). In this light, in order to correctly predict deformation effects on drop trajectory it is not sufficient to assume the drag coefficient is the same as that of a drop at terminal velocity. An accurate approach should infer the level of drop distortion based on the degree of the distorting aerodynamic force expressed in terms of, for example, Weber number. This will change as the droplet moves. The potentially high Weber numbers of cast-off and impact drops ($We > 13$) suggest the possibility of drop breakup during flight.

The high levels of cast-off and impact drop deformation in flight may affect drop trajectory, and thus blood origin estimation.

Gunshot drops, the smallest of those considered, show potential for significant deformation during flight based on high We_{avg} . Breakup is predicted for bigger drops ($d > 0.1-0.5$ mm) where they possess higher velocities (> 30 m/s). Smaller gunshot drops ($d < 0.1$ mm) are expected to experience negligible deformation ($We < 3$) despite their relatively large velocities and may be approximated as rigid spheres when predicting their trajectories.

Initial drop oscillation and deformation during flight may have significant effects on the overall drag force. These factors need to be considered in order to accurately predict blood drop origin and drop trajectories prior to impact on a surface.

This paper describes the development of a numerical scheme to accurately predict blood drop behavior during flight. The proposed

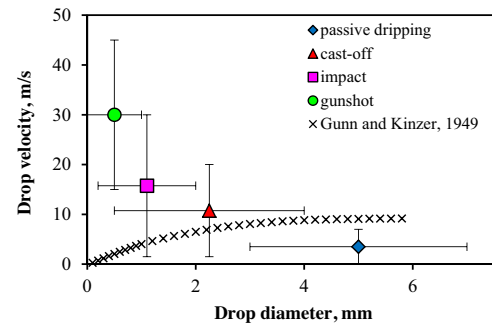


Fig. 1. Blood drop velocities versus sizes relative to the terminal velocity data for water drops (Gunn and Kinzer, 1949).

scheme incorporates the effects of inertial, gravitational and aerodynamic drag forces on drop flight. The variation in drag force as a result of shape oscillation and deformation due to aerodynamic forces are also features of this scheme. The most likely mechanisms of drop breakup during flight are also included.

The proposed scheme can predict drop flight characteristics and paths in both ‘forward’ (from the drop origin till its impact on a surface) and ‘backward’ (from the drop position on the target surface to its origin) modes, and in both 2D and 3D cases. Among the output parameters are drop 3D coordinates and velocity along the flight trajectory, impact angle and velocity, range and height of drop flight.

This paper deals with the description and validation of the numerical model for “forward” blood drop trajectory prediction, where the initial size and velocity are known. The feasibility of the “backward” trajectory prediction, where the trajectory is tracked back from a dry stain, will be addressed in future publications.

3. Numerical scheme description

To compute the trajectory of a drop, time was divided into steps. The forces on the drop (including gravity, air resistance and buoyancy) were estimated at each time-step. The change in velocity and distance traveled were calculated for each time-step and droplet position and speed updated before the next time-step.

3.1. Equation of drop motion and numerical solution

Blood drops were modeled using a Lagrangian approach, by applying Newton’s Second Law to an individual drop traveling through air with density ρ_{air} :

$$m\vec{a} = \vec{F}_g + \vec{F}_b + \vec{F}_d \quad (1)$$

Here $m = (\pi/6)d_o^3\rho$ is the mass of a blood drop with density ρ and equilibrium (undistorted) diameter d_o . $\vec{F}_g = m\vec{g}$, $\vec{F}_b = (\pi/6)d_o^3\rho_{air}\vec{g}$ and $\vec{F}_d = -(1/2)C_dA\rho_{air}V_{rel}|\vec{V}_{rel}|$ are gravitational, buoyancy and air resistance forces respectively. The buoyancy force is negligible, for a blood drop in air, but is nevertheless included. A is the drop’s projected area that faces the flow, and $C_d = f(Re)$ is its drag coefficient as a function of Reynolds number ($Re = V_{rel}d_o/\nu_{air}$). $V_{rel} = \vec{v} - \vec{u}$ is the drop velocity (relative to the air), where \vec{u} is the incident (free) stream velocity, whereas, $\vec{v} = (v_x, v_y, v_z)$ is the drop intrinsic velocity with angles to x -, y - and z -axes α , β and γ respectively (see Fig. 2).

¹ It should be noted that from terminal velocity experiments drops as large as 10 mm in diameter survive their terminal velocity conditions without disintegration ([27]). In addition, for water drops, van Boxel [59] showed that only small drops ($d < 1$ mm) would reach 95% of their terminal velocities when falling less than 2 m from rest (at the point of formation). Larger drops need larger distances to reach terminal conditions. For example, for a 2 mm drop to attain 95% of its terminal velocity of 6.49 m/s it needs to fall 5.8 m.

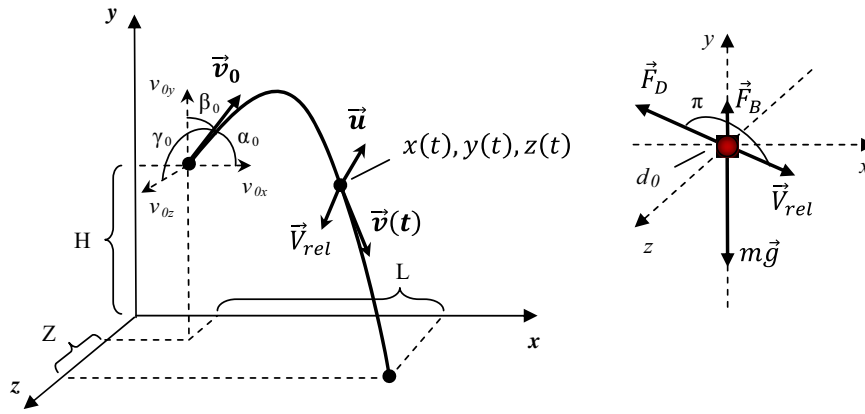


Fig. 2. Drop trajectory segment (left) and force balance segment diagram (right): initial drop velocity v_0 with initial inclination angles α_0, β_0 and γ_0 ; L, H and Z are the lengths of drop trajectory along coordinate axes.

For the components of drop acceleration Eq. (1) gives the following^{2,3}:

$$a_{x,z} = \frac{dv_{x,z}}{dt} = -\frac{1}{2m} C_d A \rho_{air} \vec{V}_{rel,x,z} |\vec{V}_{rel}| \quad (2)$$

and

$$a_y = \frac{dv_y}{dt} = -\frac{g(\rho - \rho_{air})}{\rho} - \frac{1}{2m} C_d A \rho_{air} \vec{V}_{rel,y} |\vec{V}_{rel}| \quad (3)$$

The sign of the drop relative velocity \vec{V}_{rel} was inverted in the equations for drop acceleration for the reverse (“backward”) projection using the symmetry of Newton’s second law with respect to inversion of time (a substitution of time direction from t to $-t$).

The set of first-order ordinary differential equations (ODEs) for drop velocity components (Eqs. (2) and (3)) were solved numerically at each time step using the fourth-order Runge–Kutta algorithm implemented in the C++ programming language. The same routine was employed to find the solution of the equations for the drop Cartesian coordinates. The computing time required for each simulation was typically 10 s with the time step $\Delta t = 10^{-3} - 10^{-5}$ s. The time step was determined based on a solution convergence criterion of six orders of magnitude (10^{-6}). For drop oscillations modeling each period of oscillations (T) was represented by at least 100 time steps ($\Delta t = T/100$).

4. Drop deformation models

The blood drop was considered to deform into an oblate or prolate spheroid (ellipsoid of revolution about its minor or major

² The model considered translational motion of axisymmetric drops, thus the lift force was neglected. The majority of blood drops imaged in the course of this study fitted these criteria. Lift force is important for the case of irregularly deformed drops and rotational motion.

³ In general, for a particle during its accelerating (transient) motion, the additional virtual mass force and Basset history force should also be considered [60]. However, due to the relatively high density ratio of blood (or water) to that of air ($831 < \rho/\rho_{air} < 880$) the virtual mass term may be neglected. The Basset history term is not generally negligible, however, due to its complexity, difficulty in implementation and more pronounced effects for the movement at high acceleration, it was not considered. Evaluation of the magnitude of Basset force in different multiphase flow applications can be found in Liang and Michaelides [61]. These authors found that the Basset force may be neglected in the particle equation of motion only when the fluid to particle density ratio is very high (gas bubbles in liquids) and the particle diameter is greater than 1 μm . For movement with high acceleration however, the Basset term can exceed the Stokes’ term by as much as a factor of two. These conditions are not thought to be met for typical BPA drops.

axes) [20] when subjected to a deforming aerodynamic force (Fig. 3).

The level of drop deformation during flight is believed to be influenced by both the intensity and the rate of change of the applied aerodynamic forces. A drop responds differently in the case of slow, gradual loading (as in free fall), compared to sudden or impulsive loading (e.g. shock wave disturbance).

In practice, the aerodynamic loading of the drop varies as its relative velocity changes during accelerated motion. In light of this three alternative models for the modeling of drop distortion during flight were incorporated in the present scheme.

Two of these included correlations for the aspect ratio of a deformed drop (AR), as a measure of its distortion, at steady terminal conditions, when drag force on a drop is balanced by its weight with either $AR = [4/17((17Bo/4) + 1)^{1/2} + (13/17)]^{-3/2}$ [28], where $Bo = \rho g d_0^2 / 4\sigma$, or $AR = (1 + 0.07We^{1/2})^{-3}$ [23] with $We = \rho_{air} V_{rel}^2 d_0 / \sigma$.

The models were assumed to be suitable for relatively large drops that are moving with velocities lower than their terminal velocities (e.g. passive drops) as an extreme case of maximum possible deformation.

The third model for drop deformation was based on the Taylor Analogy Breakup (TAB) model for low-Weber number sprays [29]. The model is based on an analogy between an oscillating and

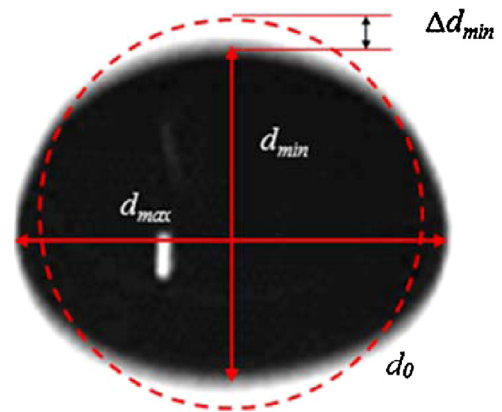


Fig. 3. Diagram of a deformed drop with the diameters of major (perpendicular to the direction of drop motion) and minor (parallel) axes of the deformed drop d_{max} and d_{min} and its shape at equilibrium (the volumes of an undisturbed and deformed drop are $V_0 = (\pi/6)d_0^3$ and $V = (\pi/6)d_{max}^2 d_{min}$ respectively. From volume conservation considerations (assuming no significant evaporation occurs): $d_0^3 = d_{max}^2 d_{min}$. The aspect ratio and cross-sectional (projected) area of a deformed drop are $AR = d_{min}/d_{max} = d_0^3/d_{max}^3$ and $A = \pi/4 d_{max}^2 = \pi/4 d_0^2/d_{max}^2$).

distorting drop and a spring mass system. The droplet distortion is represented as a one-dimensional harmonic oscillation *under the deforming aerodynamic force*, restoring surface tension force and damping viscous force.⁴ The droplet deformation in the direction of flow is expressed in terms of the dimensionless distortion $y = 2\Delta d_{min}/(d_o/2)$, where Δd_{min} describes the deviation of the minor drop diameter (or the one parallel to the direction of the flow or drop relative velocity) from its undisturbed value d_o (see Fig. 3).

The equation of motion of the deformation and a general solution are⁵

$$\frac{d^2 y}{dt^2} + \frac{4C_d \mu}{\rho d^2} \frac{dy}{dt} + \frac{8C_k \sigma}{\rho d^3} y = \frac{4C_f \rho_{air} V_{rel}^2}{C_b \rho d^2}$$

and

$$y(t) = We_c$$

$$+ e^{-t/\tau_D} \left\{ (y_o + We_c) \cos \omega t + \frac{1}{\omega} \left(\frac{dy_o}{dt} + \frac{y_o - We_c}{\tau_D} \right) \sin \omega t \right\}$$

Here $We_c = We(c_f/c_k c_b) = (\rho_{air} V_{rel}^2 d/2\sigma)(c_f/c_k c_b)$, natural frequency and damping time of drop oscillations are $\omega = \{(8C_k \sigma/\rho d^3) - (1/\tau_D^2)\}^{1/2}$ and $\tau_D = (\rho d^2/2C_d \mu) \cdot C_b = 1/2$, $C_d = 10$, $C_k = 8$ and $C_f = 2/3$ (gradual loading) or $1/3$ (sudden loading) are empirical model parameters. The initial values of distortion y_o and distortion rate of change dy_o/dt are usually taken to be equal to zero [30]. The drop aspect ratio and projected area are thus $AR = (1 - 0.5y)^{3/2}$ and $A = \pi d^2/4(1 - 0.5y)$ respectively.

The numerical representation of the drop distortion and distortion rate used for the code development are given in Appendix A.

4.1. Drag coefficient of a deformed drop

There are a number of possibilities of how to express the drag coefficient as a function of drop shape and Re number [21,30–32]. An initially spherical drop in an external flow at critical conditions reaches a maximum deformation when it takes the form of a disk (so-called ‘liquid disk’). The drag coefficient of a deformed drop can be estimated by interpolating between that of a sphere C_D^{sph} and of a disk C_D^{disk} [21,32]: $C_D = AR C_D^{sph} + (1 - AR) C_D^{disk}$. For a sphere $AR = 1$, whereas, for a thin disk $AR \approx 0$.

The empirical expressions for the drag coefficient of a solid sphere and disk for wide range of Reynolds numbers used in this study can be found in [20,33] and are given in Appendix B.

5. Drop breakup models

As soon as the maximum deformation is reached and the droplet is disk-like, a drop may further deform and finally disintegrate into smaller or child drops [23]. Two breakup mechanisms, namely bag-type at $12 \leq We \leq 50$ and vibrational at $We \leq 12$ breakup, are characteristic for typical blood drops. Two other mechanisms, multimode and shear breakup, may occur for gunshot drops if conditions of $We > 50$ are encountered.

Two alternative models for drop breakup modeling were built into the developed numerical scheme to estimate the level of drop deformation prior to the breakup.

The first was based on the experimental findings of [23] for drops disintegrating after a shock wave disturbance. In the proposed model a drop was considered to undergo breakup when the droplet Weber number is larger than a critical Weber number $We_{cr} = 12(1 + 0.077Oh^{1.6})$ ([1,32]; [23]).

The model suggests that the maximum cross-sectional drop deformation is $d_{max} = d_o(1 + 0.19We^{0.5})$. The instantaneous cross stream drop diameter d_c is estimated as a function of time t of drop deformation from the liquid disk distortion up to a drop breakup in a form $d_c = (d_{max} - d_o)0.625(t/t^*) + d_o$, where $t^* = (d_o/V_{rel})\sqrt{\rho/\rho_{air}}$ is the characteristic time of drop breakup for $Oh < 0.1$. It is assumed that the maximum drop deformation is reached at $t_i = 1.6t^*$. After that, a drop undergoes further irregular deformation (into a liquid bag, for example) and finally disintegrates. The time of drop breakup from the beginning of the deformation to drop's final disintegration is represented as $t_{bup} = 6t^*(We - 12)^{-0.25}$ for $12 < We \leq 18$ and $t_{bup} = 2.45t^*(We - 12)^{0.25}$ for $18 \leq We < 45$ at $Oh \leq 1$ [1].

The deformed drop aspect ratio and projected area are $AR = d_o^3/d_c^3$ and $A = (\pi/4)d_c^2$ correspondingly. Thus the model allows estimation of the instantaneous drop deformation at a time after the drop breakup condition had been met, hence allowing a prediction of when final breakup occurs.

For the typical case of bag-type breakup, actual drop disintegration was expected to occur anytime in the second half of the interval from t_i to t_{bup} . In the numerical implementation of the model, a random time of breakup in a characteristic time frame is calculated using random number generator $\text{rand}()$ in C++.

The final drop cross-sectional diameter was calculated subsequently. Using this distortion value, a final drop velocity and coordinates were calculated.

Another drop breakup model employed was based on the breakup model which is part of the TAB model. For this the amplitude of undamped drop oscillations was first calculated with

$A = \sqrt{(y^n - We_c)^2 + ((1/\omega)(dy/dt)^n)^2}$ where y^n and $(dy/dt)^n$ are the dimensionless drop deformation and deformation rate at n th time step. Drop breakup was considered to be possible only if $We_c + A > 1$ and $y \geq 1$.

The drop was assumed to maintain its level of deformation (aspect ratio) as soon as it reached its critical deformation, up until the completion of the breakup.

If the condition for drop disintegration was met, the lifetime of an unstable drop was calculated alternatively as $t_{bup} = 0.82\sqrt{3\rho d_o^3/8\sigma}$ [29] and $t_{bup} = \pi\sqrt{\rho d_o^3/16\sigma}$ [34] or according to [1] discussed earlier. Pilch and Erdman's expression for the drop breakup time was found to be the most accurate in predicting blood drop breakup.

If $t_{bup} \leq \Delta t$ the breakup was considered to occur during the current time step. However, if $t_{bup} > \Delta t$ the breakup would not occur during the current time step and the drop distortion and distortion rate are recalculated on the next time step $n+1$ (Appendix A).

6. Experimental methodology

6.1. Blood used

For the study of blood drops falling from up to 8 m, healthy donor human blood with EDTA anticoagulant was used. Blood density was determined by the weighing method to be $1028 \pm 25 \text{ kg/m}^3$. Blood viscosity and surface tension were not

⁴ The important limitation of the TAB model is that only the longest-lived fundamental (spheroidal or prolate-oblate) mode of drop oscillations is accounted for. This is reasonable as the low-viscosity drop oscillations are generally limited to the first few harmonics due to rapid damping of higher harmonics. Several non-linear TAB model extensions have been recently developed by Schmehl [32] and claimed to be more accurate in large drop distortion prediction. These may be used for blood drop applications if higher level of accuracy is required.

⁵ The equation of motion of the deformation for the case of ‘backward’ drop motion had the sign of the first time derivative from drop distortion y reversed.

measured. It was expected, however, that due to the fact that the blood used was of a healthy donor its viscosity and surface tension were within the range reported for healthy humans [35–37].

To investigate the early stage of passive blood drop flight for drops falling up to 1.5 m porcine blood, sourced from a slaughterhouse was used as a human blood substitute. Blood from the same sample was used for impact spatter experiments. The blood was treated with ACD (acid citrate dextrose) anticoagulant at a concentration of 7 mg/ml. Measured blood density and surface tension were $1033 \pm 20 \text{ kg/m}^3$ and $61.7 \pm 0.8 \text{ mN/m}$ correspondingly. Blood viscosity was measured to $4.6 \pm 0.1 \text{ mN s/m}^2$ at high shear rate (1000 s^{-1}) and to $21.3 \pm 0.6 \text{ mN s/m}^2$ at low shear rate (10 s^{-1}). Blood density was measured by a weighing syringe method. Surface tension measurements were performed on a KSV Contact Angle and Surface Tension Meter. Blood viscosities were measured at a shear rate of 1000 s^{-1} with a rotational rheometer HAAKE Rotovisco RV 20 with NV coaxial cylinders. ACD treated abattoir porcine blood with density, surface tension and high-shear rate viscosity of $1054 \pm 25 \text{ kg/m}^3$, $63.8 \pm 1.6 \text{ mN/m}$ and $5.0 \pm 0.7 \text{ mN s/m}^2$ respectively was used for the cast-off experiments. The blood used for each of the experiments was warmed to $36 \pm 1^\circ\text{C}$ and agitated by a magnetic heater-stirrer before testing. It was stored at 4°C and used within 4 days.

6.2. Blood drop generation and imaging

High-speed imaging was used to study passive, cast-off and impact blood drop flight characteristics. A Photron SA1.1 high speed digital (CMOS) cameras with a Nikon 55mm f/2.8 AIS Micro-NIKKOR macro lens were used to capture high resolution (with fine details) images of blood drops at high frame rates, the number or frequency of images or frames taken per second (fps). Camera settings and image magnification levels (distance calibration, number of image pixels per 1 mm) employed for the imaging experiments performed are summarized in Table 2. Photron FASTCAM Viewer Ver.3.0 (Photron Ltd.) software was used to operate the camera.

6.3. Passive drops

To study blood drops at velocities close to terminal, drops in the range of 3–5 mm in diameter were produced using Pasteur pipettes with different tip sizes. The drops were then released from a number of heights indoors to limit the effects of air currents and winds on drop flight. Ambient temperature was $21 \pm 1^\circ\text{C}$. Each meter of drop flight (starting at 2 m of fall) was imaged. The fall distance of the drops was measured with a tape measure to within $\pm 5 \text{ cm}$. A set of close-up videos of drops were also captured to measure drop diameters. Each test was repeated three times. The experimental set up was back- and side-lit from both sides by 0.5–2 kW incandescent lamps. A distance calibration (pixels/mm) was made using an image of a 1 m long ruler. The ruler was mounted vertically in the field of view of the camera. Both the ruler and falling drops were expected to be within the camera depth of field.

For the study of initial blood drop oscillations a Gilson Minipuls 3 M312 (Gilson Ltd.) peristaltic pump was used to draw the liquid from a reservoir flask to the experiment. A constant flow rate of $0.10 \pm 0.02 \text{ ml/s}$ (measured by weighing) was maintained. Blood drops were formed by dripping from a number of stainless steel objects to produce a range of drop sizes. These included a 21G Ø0.8 mm blunt hypodermic needle, SWAGELOCK[®] hose connector with a 5 mm outer tube diameter, a kitchen knife and a 100 mm diameter cylinder. The objects were at ambient temperature of $19.0 \pm 0.5^\circ\text{C}$.

The drops were allowed to fall 1.5 m in total. Owing to the image magnification necessary to accurately determine drop size and shape, 10 cm of drop flight was imaged at a time. Drop fall distance was measured to $\pm 5 \text{ cm}$. Drop images upon its formation, and after 20, 50, 100 and 150 cm of fall were taken with 10–15 repeats. The set up was back-lit with 8 LED lights.

6.4. Cast-off drops

Cast-off drops were generated from a 60 cm diameter flat rotating stainless steel disk [38]. The disk rotated clockwise about its symmetry axis, with the plane of the disk vertical. The speed of rotation was regulated by a single phase AC motor with a variable speed drive, with tangential velocity in the range of 1–20 m/s within 0.5 m/s.

A KNF Flodos diaphragm pump NF 60 was used to eject 2 ml of blood on the rotating disk surface for each experimental trial. The blood was fed onto the disk surface, at the lower part of the disk $\sim 1 \text{ cm}$ from the edge.

The drops back-lit with eleven high-intensity LED lights were imaged in flight. The drops were observed to move in the plane of the disk with maximum deviation of about ± 1 –1.5 cm. The camera was focused on the plane of the disk. Only the drops that stayed in focus until they left the field of view were analyzed.

A set of experiments with close-up imaging were performed to study the initial phase of cast-off drop flight including shape oscillations. The recorded trajectory during close-up imaging was limited to less than 4 cm. It was experimentally difficult to determine drop sizes and track any shape changes over a meaningful length of trajectory and number of oscillation periods for the smaller cast-off drops generated at the higher tangential velocities (> 6 –7 m/s). Thus the study was limited to the lower tangential velocities.

Additional experiments were dedicated to capturing longer drop trajectories to allow a comparison with the numerical predictions. The typical field of view for these experiments was about $55 \text{ cm} \times 55 \text{ cm}$ which corresponded to 60–70 cm length of imaged drop trajectory. However, the resolution was decreased to about $30 \text{ cm} \times 30 \text{ cm}$ (or $\sim 40 \text{ cm}$ of drop trajectory) at disk tangential velocities higher than 15 m/s in order to accurately determine blood drop size.

6.5. Impact drops

The generation of blood drops as a result of a blunt force impact was studied. A pneumatic cylinder (actuator) drove a piston and

Table 2
Camera settings and typical image magnification used for passive, cast-off and impact blood drop imaging.

Experiment	High-speed camera settings			Typical image magnification, pixels/mm
	Frame rate, fps	Resolution, pixels	Shutter speed, s	
Passive drops falling up to 8 m	5000	256×1024	1/6000	0.8–1 (close-up) 14–16 (drop flight)
Initial passive drop oscillations	5400	1024×1024	1/75,000	8–10
Cast-off drops	5400	1024×1024	1/75,000	9–15 (close-up) 2 (drop flight)
Impact spatter	5400	1024×1024	1/75,000	5–9

the attached rod to vertically impact a target surface. The target was a 5 cm diameter polyurethane block with a flat impact surface. The actuator and target were firmly mounted on a durable 6 cm thick wooden bench. The stroke length was about 7 cm. The rod tip was fitted with a 2 cm diameter steel tip, similar to a 16 oz. claw hammer head. The impactor tip speed at time of impact varied from 9 to 14 m/s.

2.0 ± 0.2 ml of blood was applied on the target for each experiment. A $32 \text{ cm} \times 32 \text{ cm}$ region close to the point of impact was imaged. The drops were back-lit with 5 LED lights.

The impact of the tip onto the pool of blood caused the blood to disintegrate into a dense mist of drops, moving radially outward from the impact center. Only drops which passed through a 5 mm wide vertical slit between the point of impact and imaged region were recorded to eliminate drop movement perpendicular to the camera object plane.

The images of all passive and cast-off drops were processed using MATLAB® based particle identification and tracking software. After conversion to grayscale, the images were binarized (recognized as bright objects on dark background) using a threshold value of 80–100 gray levels.⁶ The drop image properties such as coordinates, diameter and aspect ratio were measured. The droplets were then tracked over time using [39] implementation of the IDL particle tracking algorithms developed by [40]. Drop velocity was calculated from a drop displacement (Δ) during two subsequent frames and video frame rate (FR) as $\Delta \cdot \text{FR}$. Impact blood drop images were processed using ImageJ, a public-domain Java image processing and analysis program. The drop flight paths were manually recreated with ROI Manager in ImageJ.

7. Verification and validation

The developed numerical code was verified and validated against a number of analytical and experimental datasets of spherical and deformable drop flight, with particular attention to sizes and velocities relevant for typical blood drops.

A number of subroutines of the developed code needed to be validated, namely:

- (1) drop velocity and coordinates calculation;
- (2) drag coefficient of a deformed drop representation;
- (3) drop deformation, oscillation and breakup modeling.

The accuracy of the drop equation of motion solution and drop deformation representation was sufficient for the validity of the developed numerical code for blood drop trajectory prediction within model assumptions (i.e. axisymmetric drop, translational motion, prolate-oblate oscillations, no evaporation or cross-winds, etc.).

The description of the validation process was accompanied with empirical observations on passive blood drop deformation, oscillations and terminal velocities, cast-off drop deformation and oscillations and impact drop deformation and breakup of value to BPA community.

7.1. Validation of drop velocity and coordinates calculation and deformed drop drag coefficient representation

In order to verify the accuracy of drop velocity components and coordinates calculation subroutines of the program it was tested against simplified cases of undeformed (spherical) drop flight with

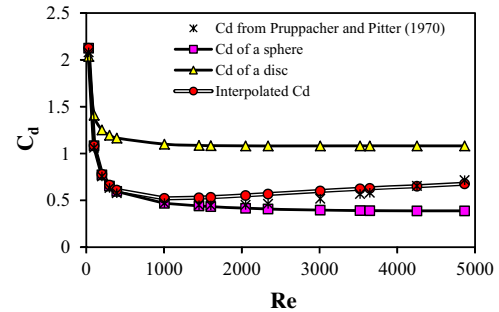


Fig. 4. Interpolated and experimentally obtained [41] drag coefficients for drops at terminal velocities with the sphere and disk drag coefficients from Clift et al. [20] and Massey et al. [33].

and without air resistance. The numerical results were found to match exactly the analytical solutions of the kinematic equations of drop motion without air resistance for:

- (1) a projectile launched horizontally from height H with initial velocity components $v_{ox} = v_o, v_{oy} = 0 : v_x = v_o, v_y = gt; x = v_o t, y = gt^2/2$; with final flight time $T = \sqrt{2H/g}$ and range $L = v_o T$;
- (2) a projectile launched under the initial angle to horizon α_o and velocity $v_o : v_x = v_o \cos \alpha_o, v_y = v_o \sin \alpha_o - gt; x = v_o t \cos \alpha_o + x_o, y = v_o \sin \alpha_o - gt^2/2$;
- (3) spherical drop flight at terminal conditions (when drag force is balanced by the drop weight) in ambient air with terminal velocity $v_t = \sqrt{(4d_o g / 3C_d)((\rho - \rho_a) / \rho_a)}$, $C_d = 0.5$.

The drag coefficient interpolation used for deformed drop representation was probed against experimentally obtained drag coefficients and aspect ratios of water drops at terminal velocity from Pruppacher and Pitter [41] (Fig. 4). This showed the good accuracy of the interpolation formula used.⁷

7.2. Validation of the models for drop deformation, oscillations and breakup

7.2.1. Passive blood drop deformation at terminal velocity

The models of drop deformation (based on Green [28], [23] and the TAB model) reproduced empirical terminal velocities and deformation levels of water drops within less than 10% for drops up to 5 mm in diameter (Fig. 5). The most accurate fit to the experimental data was provided by the TAB model with an aerodynamic force coefficient $C_f = 2/7$ over the entire range of drop diameters studied. The models based on Green [28] and [23] predicted terminal velocities higher than reported experimentally for water drops with diameters >6 mm. The TAB model and that based on [28] provided a good approximation of drop deformation levels at terminal conditions for a wide range of drop sizes. The HF model, however, overestimated drop deformation for drops less than 8 mm in diameter.

The validity of the code when predicting blood drop flight at conditions close to terminal was tested against experimental data on drops falling from up to 8 m.

From close-up drop images, falling drop diameters with standard deviations were 3.31 ± 0.01 mm ('small'), 4.44 ± 0.05 mm ('medium') and 4.94 ± 0.04 mm ('large'). The error in drop diameter measurement associated with image pixelation and thresholding was estimated to be

⁶ Kabaliuk [62] contains additional information on the effect of threshold values on the measured drop diameter.

⁷ The interpolation is valid provided the validity of drop deformation representation irrespective of the specifics of drop movement (or drop type in BPA context).

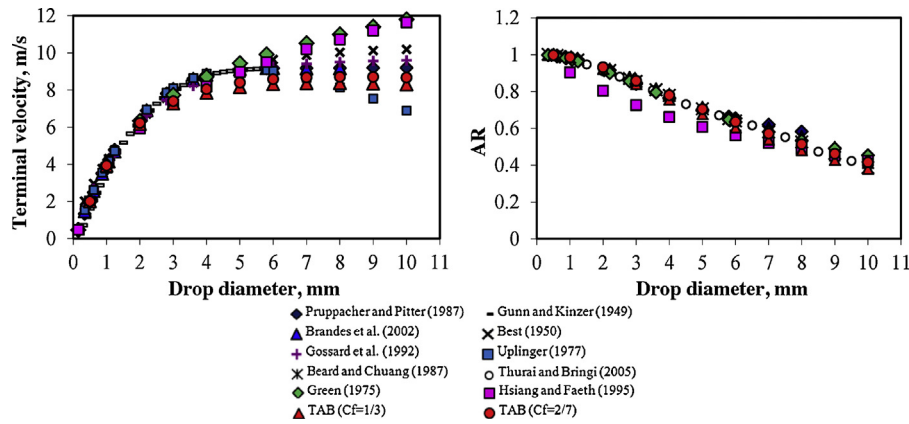


Fig. 5. Comparison of numerical and empirical terminal velocities and corresponding deformation levels for water drops. The lower four data sets represent numerical predictions. [50–54]

± 3 pixels (or ± 0.2 mm) for close-up images. The accuracy of drop diameter determination for drop flight videos was limited by image resolution, which amounted to 1 pixel size (or ± 1 mm).

The velocity of the falling drops was observed to increase from about 5–6 m/s at 2 m of fall to 8–9 m/s at 9 m. The time-dependent evolution of falling drop velocity for the larger drops studied was plotted in Fig. 6. Scatter of ± 3 –4 m/s observed in the raw data was associated with an uncertainty in drop location (center of mass) determination from pixilated and thresholded images of ± 5 m/s.

Drop fall analogous to that studied experimentally was modeled using the developed code. The experimentally measured blood drop size and density were used for computation. As the viscosity and surface tension of the blood were not measured, published values of human blood viscosity of 4 mN s/m² (at high shear rate) and surface tension of 62 mN/m ([35,37]) were used.⁸

All the models for drop deformation during flight (based on Green [28],[23] and TAB) performed well when predicting drop fall velocity and consequently drop deformation levels which affect drag force and drop trajectory (or velocity in the case of drop fall). Numerical velocity predictions were within 5% of the mean of the experimental data.

Numerical simulation for the case of a spherical blood drop (“No deformation” dataset) with a drag coefficient dependent on Reynolds number predicted higher drop velocities compared to the models with drop deformation, and higher than the experimental mean, although within the scatter of experimental data. The discrepancy, however, was observed only for fall distances higher than about 4 m.

When the drag force was entirely neglected (“No drag” dataset), the predicted velocities deviated substantially from those of a droplet experiencing drag by the time it had fallen 1.5 m. It is rare for a passive blood drop to fall (vertically) much more than 1.5 m at a crime scene. Such a short travel distance (and time of flight) would not allow a passive drop to experience any significant drag force effects and deformation to alter its flight velocity (and thus, impact velocity) under typical crime scene conditions.

⁸ It should be pointed that a change in simulated blood drop viscosity over the range of its natural variability caused no detectable difference in blood drop fall velocity (less than 1/10,000%). A decrease in drop surface tension from 62 to 55 mN/m led to a less than 2% decrease in drop fall velocity. Measured blood density was slightly lower than published values. However, from the simulation a 3% increase in drop density from measured 1028 to 1063 kg/m³ (upper level for human blood) increased drop velocity only by about 1%.

7.2.2. Initial oscillations of passive blood drops

The early stage of passive blood drop flight was also experimentally and numerically studied. Initial oscillation amplitude and damping rate for drops falling up to 1.5 m were investigated.

The drops formed from the objects tested ranged from 1 to 6 mm in diameter (see Table 3). Blood dripping from the hypodermic needle and kitchen knife generally produced uniform-size drops (main or primary drops). For the case of a dripping hose connector and cylinder, the primary drop was followed by one or rarely two (or more) smaller droplets (termed ‘accompanying drops’ or ‘satellite drops’). Initial oscillations of the needle, knife, hose connector and cylinder primary drops as well as uniform-sized hose connector satellite drops were investigated.

The primary drops were tracked as soon as the breakup from the ligament was commenced and the body of a drop could be differentiated from the residual liquid adhering to the dripping surface. Upon formation the drops experienced shape oscillations with axisymmetric mode predominating.

The satellite drops studied were formed as a result of the break-off a highly elongated liquid ligament (length to width ratio of about 10) from the residual liquid and its subsequent strong contraction. The presence of a horizontal oscillation mode (see [42]) was noticed for the first ten to fifteen frames (or about 5 mm). This may be attributed to the mode-coupling phenomena noted by [47].

Most of the passive blood drops possessed a prolate shape upon detachment, whereas the drops formed from the cylinder were oblate (at the time of recognition).

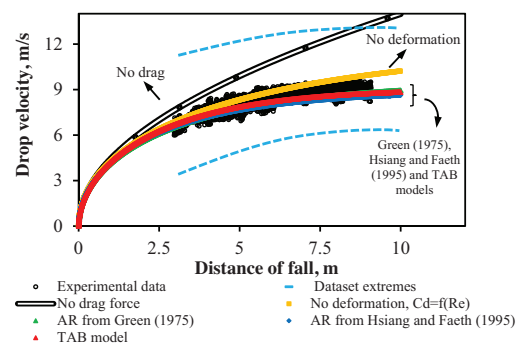


Fig. 6. Empirical and numerical fall velocity of a Ø4.94 mm passive blood drop. The dataset extreme line was fitted through the measured velocity data extreme points. The black points are the moving average of the processed data.

Table 3

Passive blood drop diameters for initial blood drop oscillation study. The error in drop diameter measurement due to image pixilation and thresholding was ± 1 pixel (or ± 0.11 mm).

Dripping object	Drop diameter, mm	Standard deviation, mm
Needle	2.83	0.01
Knife	3.96	0.11
Hose connector		
Primary	5.34	0.06
Satellite	1.25	0.08
Cylinder	5.83	0.15

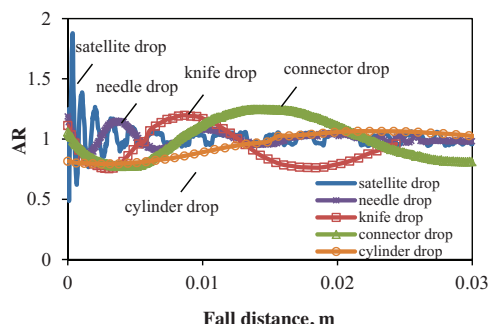
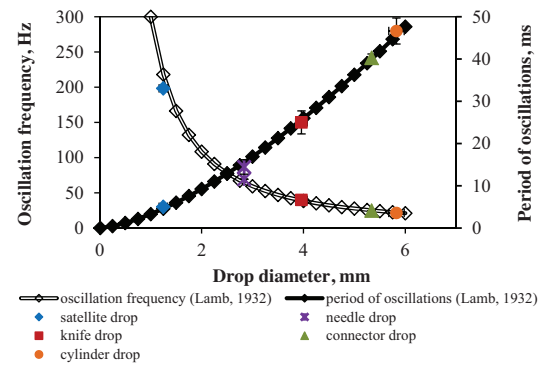
Aspect ratios of the representative oscillating drops were plotted in Fig. 7 for the initial stages of flight where drop deformation by aerodynamic forces is less prominent due to low Weber numbers ($We \ll 1$). The drops oscillated around a spherical shape ($AR \approx 1$) with viscous damping reducing the amplitude and the shape tending to spherical over time.

The mean error in drop aspect ratio determination from ellipse-fitting was less than 1%. It should be noted that the fitting error for the first ten frames of the strongly deformed satellite droplet reached 3%, but reduced for the following images. The uncertainty in drop location determination from the high-speed images was ± 1 mm.

The primary drops experienced moderate- to small-amplitude oscillations with the dimensionless drop distortion $y < 0.4$ and $|1 - AR| \leq 0.3$. The satellite drops oscillated with higher amplitudes ($y \leq 0.8$ and $|1 - AR| \leq 0.9$).

A comparison of the measured period and frequency of drop oscillations with theoretical predictions by ([43]; cf. [44]) for small-amplitude oscillations of a low-viscosity liquid drop in air is provided in Fig. 8. The oscillation frequency and decay time for the fundamental harmonic are $\omega = \{(64\sigma/\rho d_0^3) - (20\mu/\rho d_0^2)^2\}^{1/2}$ and $\tau_D = (\rho d_0^2/20\mu)$. Surface tension increases drop oscillation frequency as $\sigma^{1/2}$. The effect of an increase in drop density is mainly due to an increase the oscillation decay time and to a decrease in oscillation frequency proportionally to $\rho^{-1/2}$. The drop viscosity μ decreases the natural oscillation frequency and damps the oscillations. As blood is a non-Newtonian fluid its viscosity depends on the shear rate of the flow. To define the apparent viscosity of an oscillating blood drop in an air flow, the flow pattern and shear rates within the drop must be determined. The latter is a complex problem and was out of scope of this study.

Larger drops studied were observed to oscillate with lower frequencies and thus had longer periods. The frequency and period of oscillation of the largest drop studied (5.83 mm in diameter, from the cylinder) was about 134.7 ± 0.4 Hz and 47 ± 3 ms respectively, whereas the needle drops (half as large) had an oscillation frequency three times higher of 435 ± 1 Hz and a shorter

**Fig. 7.** Initial oscillations of passive blood drops observed experimentally.**Fig. 8.** Frequency and period of passive blood drop oscillations.

oscillation period of 14 ± 2 ms. Empirical and theoretical oscillation frequencies (and periods) were in good agreement. This is in concordance with the findings of [45] that the asymptotic behavior of small and moderate low-viscosity drop oscillations can be well predicted by the linear theory [44].

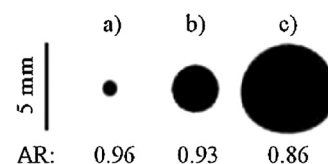
The shift in oscillation frequency of the satellite drop oscillations may be associated with the decrease in oscillation frequency of the fundamental mode with increasing amplitude [46,47]. Indeed energy transfer between the fundamental and higher modes (mode coupling) during high-amplitude oscillations changes the energy balance of the fundamental mode. Another possible explanation is the error in drop size estimation, which is critical during rapid oscillations.

As the velocity of a passive drop increases ($We \geq 1$) with the distance of fall, aerodynamic effects on drop deformation become more pronounced. The equilibrium drop aspect ratio shifts from that of a spherical drop ($AR = 1$) toward the values for an oblate spheroid ($AR < 1$). This was observed experimentally for the passive blood drops. The deformations naturally were more pronounced for the larger drops which also showed a non-elliptical profile with flattening at the bottom surface facing the flow (Fig. 9). It should be noted that the hose drops still showed some oscillations after 1.5 m of fall.

A comparison between the experimental and numerical data on drop oscillation from the moment of drop formation is presented in Fig. 10 for the hose connector drops.

The analytical solution for the free drop oscillation around a spherical shape [48] $AR = [1 + A_0 e^{-t/\tau_D} \sin(\omega t)]^{-3}$ is shown in Fig. 10. It models passive blood drop oscillation accurately up to the third period. The parameter $A_0 = 0.08$ was used to match experimentally observed drop oscillation data.

As the Weber number of drop flight exceeded 0.4 at 0.15 s of fall, drop behavior deviated from that predicted by the free oscillation theory. As the drop velocity increased due to the action of gravity the drop started to deform under the increased aerodynamic loading and oscillated around an equilibrium deformed shape. With further gradual rise in the aerodynamic loading the drop further deformed. The amplitude of oscillation was damped with time by viscous forces.

**Fig. 9.** Passive blood drop shapes and aspect ratios after 1.5 m of fall: (a) satellite, (b) needle and (c) hose connector drops. Standard deviation of the aspect ratio measurements was ± 0.3 .

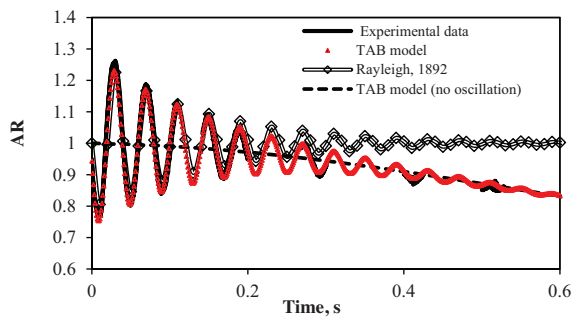


Fig. 10. Experimental and numerical results for the initial oscillation of a 5.34 mm diameter passive blood drop. Initial distortion y_0 and distortion rate \dot{y}_0 used for the simulation were 0.076 and 55 s^{-1} correspondingly).

The simulation of the initial drop oscillation based on the TAB model and empirical data on drop sizes, properties, initial distortion levels and rates provided accurate prediction of the passive drop behavior during flight beginning from the moment of its formation.

Measured blood drop density and surface tension values were incorporated into the TAB model. Variations in the blood surface tension and density in the range of the instrumental errors had negligible effect on the numerical results. The value of apparent drop viscosity was selected from the measured and published data [35,36] by matching the experimental and numerical oscillation decay times. The viscosity value of 10 mN s/m^2 (for the shear rate of 10 s^{-1}) provided the most satisfactory data fit and was used for simulations.

The maximum relative error in drop aspect ratio values predicted numerically to that observed experimentally was about 1.6% for the first period of drop oscillation which may be associated with the errors in the assumed shape of the newly formed drop.

The empirical levels of drop deformation after about 0.5 s (or 1.5 m) of fall were slightly lower ($\sim 5\%$) than those calculated numerically with the TAB model based on the critical Weber number $We_{cr} = 12$ for shock loading [23,26] with $C_f = 1/3$. To improve the agreement the value of $C_f = 2/7$, corresponding to slightly higher $We_{cr} = 14$, reasonable for a gradual increase in the aerodynamic loading, was employed in the computation. The TAB model with $C_f = 2/7$ performed well for all the primary drops studied experimentally. The relative errors in drop fall velocity and distance between the numerical approximation and experimental data was generally smaller than 0.5%.

The steady state solution (without drop shape oscillation and initial distortion) for falling passive blood drops was also investigated. It should be noted that the deviation between the numerical solutions for an initially deformed, oscillating drop and the one for initially spherical, non-oscillating drop was negligibly small ($< 1/1000\%$) when predicting the evolution of drop fall velocity, distance and time. This may suggest that the effect of drop initial oscillation and distortion from sphericity on its flight characteristics is negligibly small. Thus for all problems, other than the initial drop shape oscillation prediction, a passive blood drop can be modeled by an initially undisturbed non-oscillating drop undergoing deformation during flight under the aerodynamic forces.

7.2.3. Cast-off drop deformation and oscillations

Blood drops cast-off from a rotating disk served as a complementary validation case. Drop oscillations and deformation levels were examined.

The cast-off drops studied ranged in size from 0.4 to 4 mm in diameter and possessed velocities of 1–15 m/s. The uncertainty in drop diameter measurement due to image pixilation and thresholding was less than or equal to $\pm 0.11 \text{ mm}$ for close-up images or

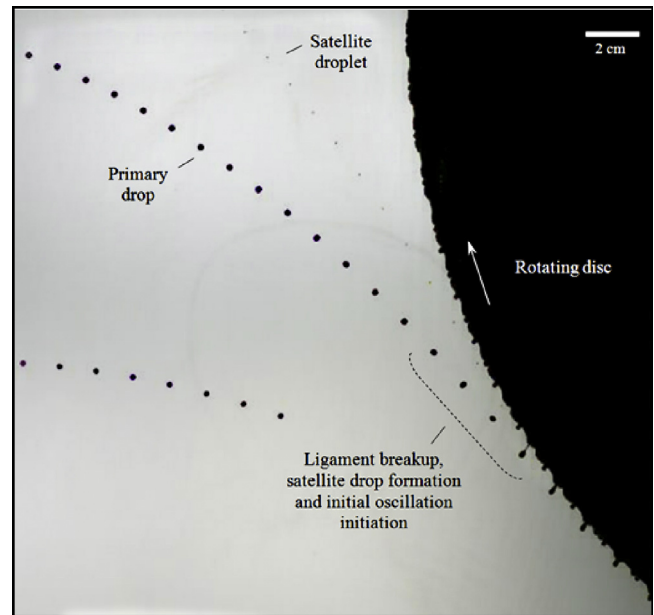


Fig. 11. Superimposition of cast-off drop images. The disk rotates clockwise.

$\pm 0.5 \text{ mm}$ for longer drop trajectory videos. The uncertainty in drop velocity measurements was $\pm 0.4 \text{ m/s}$ and less than $\pm 2 \text{ m/s}$ respectively.

A liquid mass adheres to the surface of the disk by interfacial tension forces. If these forces are weaker than the centripetal force required to keep it rotating at the disk speed, the mass will break up into drops which fly off tangentially. Gravity also acts.

The blood deposited on to the lower disk surface was observed to move to and accumulate on the disk edge. As blood accumulated at the edge, the weight of the adhering mass and the centripetal force required to keep it rotating with the disk increased. When the interfacial force was no longer sufficient, an adhering drop started to elongate and formed a liquid neck. The orientation of the liquid neck axis of symmetry changed during disk rotation and as the liquid mass increased. During the early stages of drop formation the axis was oriented perpendicularly to the tangent to the disk circumference at the point of drop contact. Later it further elongated and tilted from being perpendicular to the disk tangent. When the liquid neck narrowed enough it broke up in one or several places generally producing a primary drop and one or more accompanying or satellite drops. After the drop detached, some quantity of liquid was left adhering to the disk surface. As long as the liquid flow rate was sufficient this liquid would undergo subsequent similar stages of drop formation (see Fig. 11).

At lower disk velocities (up to about 6 m/s) the drops tended to detach from the lower part of the rotating disk whereas at higher rotational speeds (and thus higher centripetal forces required for

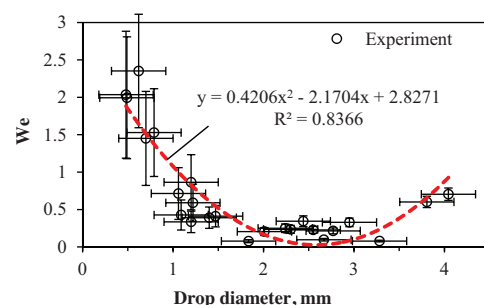


Fig. 12. Weber number for the 0.4–4 mm cast-off drops studied.

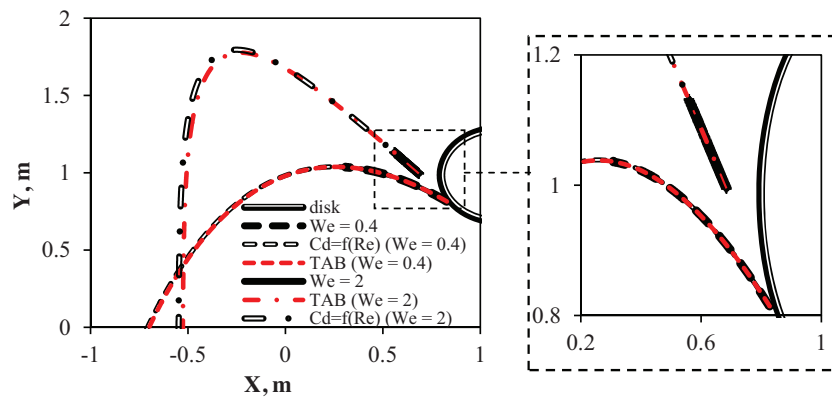


Fig. 13. Empirical (bold solid and dashed black lines) and numerical cast-off blood drop trajectories at $We = 0.4$ and 2 .

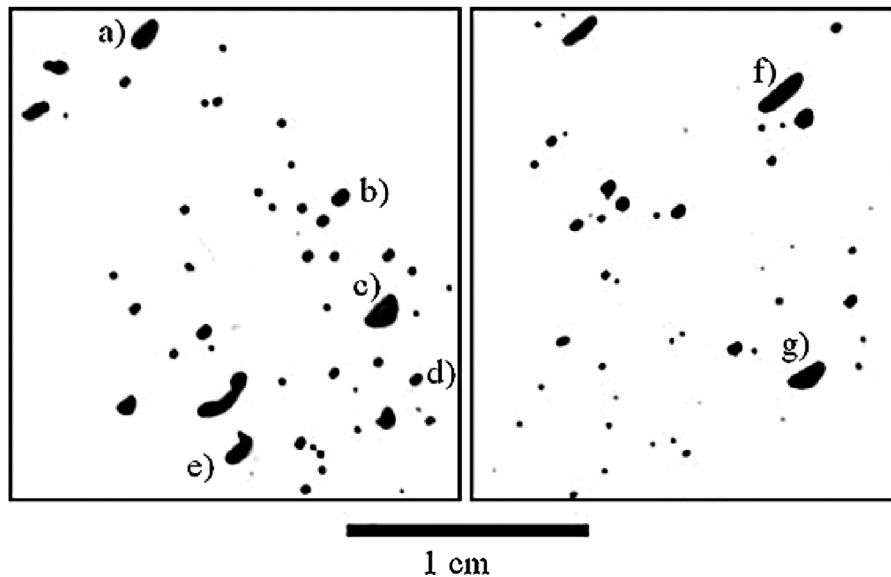


Fig. 14. Highly deformed impact drops observed: a–d = 1.4 mm, $AR = 0.67$, $We = 9.7$; b – 0.9 mm, 0.86, 5.6; c – ‘liquid bag’ 1.54 mm, 0.75, 10.4; d – 0.68 mm, 0.92, 4.6; e – 0.9 mm, 0.86, 5.8; f – 1.6 mm, 0.37, 9; g – ‘liquid bag’ 1.5 mm, 0.6, 8.4.

adhesion) the detachment region extended to the whole disk perimeter.

Once released, the primary and accompanying cast-off drops continued to move away from the disk with velocities similar to the tangential velocity of the disk. The initial trajectory was tangential to the disk.

While in flight the drops experienced shape oscillations due to the unbalanced surface tension forces at the time of release. Most of the primary cast-off drops detached with a prolate spheroidal shape (with $|1 - AR|_0 < 0.2$). They oscillated with moderate to small amplitude with the dimensionless drop distortion ($y < 0.4$ and $|1 - AR| \leq 0.3$) and damping rates within the range seen in passive dripping. This suggested that the initial oscillations of this type of drops may be successfully modeled with the numerical scheme that performed well for the passive blood drops oscillation simulation discussed above.

The size of the primary drops cast off from the disk decreased as the rotational velocity increased. The ligament length, on the contrary, increased with the speed of rotation. The longer ligaments, consequently, produced higher numbers of smaller diameter satellite drops.

As the relatively larger cast-off drops formed at lower velocities, and drops that possessed higher velocities were significantly

smaller in size, the initial Weber numbers of the cast-off drops remained low (< 3). Moreover, as each drop was formed it would decelerate (and thus the We number of its flight would decrease) due to the combined action of air resistance and gravitational force. Such low Weber numbers for cast-off drops (see Fig. 12) indicate low deformation levels during flight which are unlikely to influence the drop’s flight path and/or velocity at the moment of impact on a surface. Breakup in flight is highly unlikely.

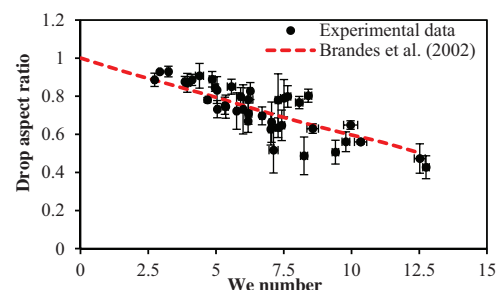


Fig. 15. Aspect ratios versus Weber numbers for impact drops studied.

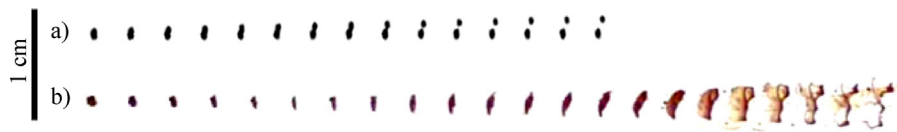


Fig. 16. Examples of vibrational (a) and bag (b) impact blood drop breakup (drop movement is from left to right).

Experimental and numerical trajectories of cast-off blood drops for representative We numbers of 0.4 and 2 were compared (Fig. 13). The Weber number of 0.4 (black dashed line) corresponded to a 1.46 mm drop with an initial velocity of 3.8 m/s, which detached from the disk rotating at 4 m/s. $We = 2$ (black solid line) was the highest We for which adequately long trajectories were captured experimentally. This corresponded to a 0.48 mm blood drop cast off from the disk rotating at 15 m/s with the velocity upon detachment of 14.8 m/s.

Numerical solutions were computed with the spherical ($C_d = f(Re)$) model and deformable (TAB model) blood drop trajectories for comparison. Both models provided an accurate prediction of the observed drop flight giving evidence of their validity, at least over the length of trajectories studied, for cast-off drop flight modeling.

The simulation was sensitive to the initial input data such as drop size, velocity and angle to the horizontal line which were measured with finite uncertainties. In order to corroborate the accuracy of the model, both drop trajectory and velocity evolution over the duration of imaging were compared to the experimental results. The maximum relative errors in drop position and velocity were less than 2%, which is within the experimental uncertainties.

When the trajectory predictions from the TAB model and the $C_d = f(Re)$ model for a spherical (undeformed) drop were continued until the moment of drop impact onto a horizontal surface ($y = 0$) for the low We number flight, the predicted drop height and range (vertical and horizontal distances traversed since separation, ~ 0.8 and 1.5 m respectively) were within 1 cm and the impact velocity was within less than 0.6%. For the higher We the numerical solution for a deformable drop predicted a shift in drop trajectory from that of a spherical drop, with faster drop deceleration. The latter resulted in a smaller flight range and lower impact velocity. The deviation, however, was less than 4% (2.2 cm) for the flight range studied (~ 1.53 m) and 0.1% for the velocity at impact.

It is, however, an item for future work to investigate the possibility of the formation of bigger cast-off drops from real sharp- and blunt-tip weapons at higher swing velocities which would possess higher We numbers and deformation levels.

7.2.4. Impact drop deformation and breakup

Impact drops studied ranged from 0.1 mm (limited by the image resolution and magnification) up to 2 mm in diameter (see Fig. 14 for examples). Measured initial drop velocities were $14\text{--}25 \pm 0.5$ m/s.

Drop aspect ratios were plotted against flight Weber numbers (Fig. 15). The aspect ratio (AR) and We numbers plotted are the average values over the first 3–5 frames of drop flight. Error bars for the aspect ratio values are equal to two standard deviations. The uncertainties in We were calculated from the uncertainties of drop size and velocity.

The correlation for the aspect ratios of drops at terminal velocities $AR = 0.9951 + 2.51 \times 10^{-2}d_0 - 3.644 \times 10^{-2}d_0^2 + 5.303 \times 10^{-3}d_0^3 - 2.492 \times 10^{-4}d_0^4$ ([49] based on Gunn and Kinzer, 1979) was plotted over the experimental data points and provided a good representation of the deformation levels of drops formed as a result of a blunt force impact. In other words, the deformational response of an impact drop was concordant with that of a falling drop under steady aerodynamic loading at terminal velocity. The behavior of drops at terminal velocity was shown earlier to be accurately predicted by all three deformation models employed, with the best fit provided by the TAB model.

About seven vibrational and eight bag-type secondary drop breakup cases were observed for the impact spatter (Fig. 16). The breakup was possible due to the presence of relatively big spatter blood drops (1–1.5 mm) which, upon formation, possessed high velocities and thus Weber numbers (11–15) larger than the critical Weber number (8–12) for drop breakup commencement ([1]; [26]; [23]). Most of the breakup cases occurred close to the impact point, within the first 10–20 cm of the spatter flight.

The drops were initially observed to deform into ‘liquid disks’ with aspect ratios of 0.3–0.4.

The latter was in good agreement with the critical deformation level for drop breakup of $y \sim 1$ (or $AR \sim 0.35$) postulated in the TAB model.

The maximum cross-sectional drop diameter (d_{max}) predicted by the [23] model was mostly within 5% of that measured experimentally (see Table 4). Drops no. 2 and 8, however, possessed slightly asymmetrical distortion which affected size and aspect ratio measurements and resulted in the discrepancy between experimental and numerical d_{max} (by about 13%) and discussed latter breakup time t_{bup} .

After the maximum drop deformation was reached, drops further deformed into a bag- or dumbbell-like shaped depending on the mode of breakup. The drops then disintegrated into smaller or child droplets. The vibrational drop breakup in the majority of cases resulted in the parent drop dividing into two approximately equally sized child drops, whereas bag disintegration produced a number of different sized droplets. Pilch and Erdman's [1]

Table 4

Empirical and numerical blood drop bag breakup time t_{bup} and maximum cross-stream diameter d_{max} comparison.

#	d , mm	V , m/s	We	Empirical d_{max} , mm	d_{max} (Hsiang and Faeth, 1992), mm	Empirical t_{bup} , ms	t_{bup} [1], ms	t_{bup} [29], ms	t_{bup} [34], ms
1	1.16	25.44	14.4	1.99	1.98	6.4	6.4	3.6	5.1
2	1.02	27.58	15.1	1.57	1.78	4.8	4.9	3	4.2
3	1.10	30.28	19.6	2.13	2.02	3.9	3.9	3.1	4.4
4	1.15	29.66	19.6	2.12	2.12	4.2	4.1	3.4	4.8
5*	1.75	24.08	19.6	3.49	3.38	7.3	7.7	6.3	9.0
6	1.59	27.27	21.6	3.02	3.01	6.1	6.2	5.4	7.7
7	1.45	28.38	22.6	2.81	2.75	4.4	4.9	4.6	6.6
8*	2.20	25.85	28.4	3.87	4.41	10.2	12.4	8.4	12.2

expression approximated the breakup time within about 10% of the experimental values, whereas [29], Reitz and Diwakar's [34] expressions predicted either lower or higher breakup time by as much as about 25%.

8. Conclusions

A numerical code for accurate modeling of blood drop flight was developed. Gravitational and aerodynamic drag forces as well as in-flight drop deformation, oscillations and possible secondary break-up were incorporated.

The validity of the code when predicting passive blood drops flight with velocity close to terminal was investigated by comparing numerical predictions and experimental data on blood drops falling from up to 8 m. All the models for drop deformation during flight performed well when predicting drop deformation levels and, consequently, drop fall velocity. Numerical velocities were within 5% of the mean of the experimental data. It was found that the deformation effects on passive blood drop trajectory may be neglected for fall distances less than 1–1.5 m which is characteristic for typical crime scene conditions.

Typical passive blood drops with diameters of $1\text{ mm} < d < 6\text{ mm}$ on early stages of flight (falling up to 1.5 m) were also experimentally and numerically studied. The simulation of the initial drop oscillation based on the TAB model provided accurate prediction of the passive drop behavior. The relative error in drop aspect ratio values predicted numerically to that observed experimentally was within 1.6%. Variations in the blood surface tension and density in the range of the instrumental errors had negligible effect on the numerical passive drop oscillations and trajectories. A blood viscosity of 10 mN s/m^2 (for the low shear rate of 10 s^{-1}) provided the most satisfactory data fit and was recommended for passive blood drop oscillations modeling.

It was also suggested that the effects of drop initial oscillation and distortion from sphericity on its flight characteristics are negligibly small, and a passive blood drop can be accurately represented by an initially undisturbed non-oscillating drop undergoing deformation during flight for all problems other than the initial drop shape oscillation modeling.

The Weber numbers of the cast-off drops studied did not exceed 3 indicating low deformation levels present and high unlikelihood of drop disintegration which is unlikely to alter their flight path and/or velocity at the moment of impact on a surface and thus the area (or volume) of origin determination. The developed numerical model provided an accurate prediction of the observed cast-off drop trajectories over the length of flight studied.

Future work is, however, required to investigate the possibility of the formation of larger cast-off drops from real sharp- and blunt-tip weapons at higher swing velocities and, thus, higher Weber numbers and deformation levels.

The impact blood drops studied possessed high levels of deformation (with aspect ratios as low as 0.4) and were observed to breakup in the vibrational and bag-type modes at $We_{crit} \approx 12\text{--}14$ within first 10–20 cm of flight.

It was shown that impact drop deformation at the studied conditions can be accurately described with the correlations for falling drops. The later were accurately represented by the developed model. The drop breakup model based on [23] predicted the critical empirical impact drop deformation levels within 5%. Pilch and Erdman's [1] expression for the time of drop breakup was found to be the most accurate when predicting impact blood drop breakup.

The deformation levels and breakup possibility and modes of gunshot spatter drops require additional investigation. The range of sizes and velocities of the gunshot spatter drops and, thus, high Weber numbers and deformation is of major interest.

Acknowledgements

We would like to thank to the Freshpork NZ Ltd. for supplying porcine blood for this study. We thank Therese de Castro, Margaret Dodds, Ken Morison, Milad Soltanipour Lazarjan and Pavlo Kokhanenko for support and encouragement. We are grateful to Bart P. Epstein for valuable and pleasant discussions. The technical stuff of the Mechanical Engineering Workshop and Laboratories contributed essential advice and inspiration. N.K. was funded by a University of Canterbury Doctoral Scholarship and E.W. by an ESR Scholarship.

Appendix A. Numerical representation of the drop distortion and distortion rate used for the code development

The drop distortion and distortion rate on the next computational time step $n + 1$ were calculated based on the distortion y^n and distortion rate $(dy/dt)^n$ on the previous time step n as

$$y^{n+1} = We_C + e^{-\Delta t/t_D}$$

$$\left\{ (y^n - We_C) \cos \omega \Delta t + \frac{1}{\omega} \left(\left(\frac{dy}{dt} \right)^n + \frac{y^n - We_C}{t_D} \right) \sin \omega \Delta t \right\}$$

and

$$\left(\frac{dy}{dt} \right)^{n+1} = \frac{We_C - y^{n+1}}{t_D}$$

$$+ \omega e^{-\Delta t/t_D} \left\{ \frac{1}{\omega} \left(\left(\frac{dy}{dt} \right)^n + \frac{y^n - We_C}{t_D} \right) \cos \omega \Delta t - (y^n - We_C) \sin \omega \Delta t \right\}.$$

The drop aspect ratio and projected area: $AR^{n+1} = (1 - 0.5y^{n+1})^{1.5}$ and $A^{n+1} = \pi d_0^2/4(1 - 0.5y^{n+1})$.

Appendix B. Empirical expressions for the drag coefficient of a solid sphere and disk

Drag coefficient of a rigid spherical particle [20]:

$$C_D^{sph} = \frac{3}{16} + \frac{24}{Re}, \text{ for } Re \leq 0.01;$$

$$C_D^{sph} = \frac{24}{Re} (1 + 0.3115 Re^{(0.82-0.05x)}), \text{ for } 0.01 < Re \leq 20;$$

$$C_D^{sph} = \frac{24}{Re} (1 + 0.1935 Re^{0.6305}), \text{ for } 20 < Re \leq 260;$$

$$C_D^{sph} = 10^{(1.6435 - 1.1242x + 0.1558x^2)}, \text{ for } 260 < Re \leq 1.5 \times 10^3;$$

$$C_D^{sph} = 10^{(-2.4571 + 2.5558x - 0.9295x^2 + 0.1049x^3)}, \text{ for } 1.5 \times 10^3 < Re \leq 1.2 \times 10^4;$$

$$C_D^{sph} = 10^{(-1.9181 + 0.637x - 0.0636x^2)}, \text{ for } 1.2 \times 10^4 < Re \leq 4.4 \times 10^4;$$

$$C_D^{sph} = 10^{(-4.339 + 1.5809x - 0.1546x^2)}, \text{ for } 4.4 \times 10^4 < Re \leq 3.38 \times 10^5;$$

$$C_D^{sph} = 29.78 - 53x, \text{ for } 3.38 \times 10^5 < Re \leq 4 \times 10^5;$$

$$C_D^{sph} = 0.1x - 0.49, \text{ for } 4 \times 10^5 < Re \leq 10^6;$$

$$C_D^{sph} = 0.19 - \frac{8 \times 10^4}{Re}, \text{ } Re > 10^6 \text{ where } x = \log_{10} Re.$$

Drag coefficient of a rigid disk perpendicular to the flow [33]:

$$C_D^{disk} = \frac{24}{Re}, \text{ for } Re < 1;$$

$$C_D^{disk} = 10^{(0.00507 - 0.05161x^4 + 0.16082x^2 + 0.01987x^2 - 0.9735x + 1.39573)} \quad \text{with} \\ x = \log_{10} Re \text{ for } 1 \leq Re \leq 2000 \text{ and } x = \log_{10} 2000 \text{ for } Re > 2000.$$

References

- [1] M. Pilch, C. Erdman, Use of break-up time data and velocity history data to predict the maximum size of stable fragments for acceleration-induced break-up of a liquid drop, *Int. J. Multiphase Flow* 13 (1987) 741–757.
- [2] SWGSTAIN BPA Terminology, 2009. Scientific Working Group on Bloodstain Pattern Analysis (SWGSTAIN) website (accessed 25.7.10).
- [3] V. Balthazard, R. Piedlievre, H. Desoille, L. DeRobert, Etude des gouttes de sang projete (Study of projected drops of blood), in: *Annual Medecine Legale Criminol Police Science Toxicology*, 22nd Congress of Forensic Medicine, Paris, France, 1939, pp. 265–323.
- [4] H.L. MacDonell, L.F. Bialousz, Flight Characteristics and Stain Patterns of Human Blood, Law Enforcement Assistance Administration, National Institute of Law Enforcement and Criminal Justice, 1971.
- [5] H.L. MacDonell, Bloodstain Patterns 1997, Laboratory of Forensic Science, New York, 1982.
- [6] T.L. Laber, Diameter of a bloodstain as a function of origin: distance fallen, and volume of a drop, *Int. Assoc. Bloodstain Pattern Analysts News* 2 (1) (1985) 12–16.
- [7] A.Y. Wonder, Blood Dynamics, Academic Press, London, 2001.
- [8] L. Hulse-Smith, N.Z. Mehdizadeh, S. Chandra, Deducing drop size and impact velocity from circular bloodstains, *J. Forensic Sci.* 50 (1) (2005) 1–10.
- [9] H.L. MacDonell, K. DeLige, On Measuring the Volume of very small Drops of Blood and Correlation of this Relationship to Bloodstain Diameter, *International Association of Bloodstain Pattern Analysts*, 1989.
- [10] P.L. Kirk, Affidavit Regarding State of Ohio V. Samuel Sheppard, Court of Common Pleas, Criminal Branch, No. 64571, 1955, April 26.
- [11] T.R. Bevel, M. Gardner, Bloodstain pattern analysis with an introduction to crime scene reconstruction, in: *Practical Aspects of Criminal & Forensic Investigations*, 3rd ed., CRC Press, Boca Raton, 2008.
- [12] N. Behrooz, Bloodstain Pattern Analysis of Determination of Point of Origin, (BSc dissertation), Department of Mechanical and Industrial Engineering, University of Toronto, 2009.
- [13] K.G. de Bruin, R.D. Stoel, J.C.M. Limborgh, Improving the point of origin determination in bloodstain pattern analysis, *J. Forensic Sci.* 56 (2011) 1476–1782.
- [14] J.K. Wells, Investigation of Factors Affecting the Region of Origin Estimate in Bloodstain Pattern Analysis, (MSc dissertation), Mechanical Engineering Department, University of Canterbury, 2006.
- [15] E.J. Podworny, A.L. Carter, Computer modelling of the trajectories of blood droplets and bloodstain pattern analysis with a PC computer, in: 2nd Training Conference in International Association of Bloodstain Pattern Analysis, 1989.
- [16] U. Buck, B. Kneubuehl, S. Nather, N. Albertini, L. Schmidt, M. Thali, 3D bloodstain pattern analysis: ballistic reconstruction of the trajectories of blood drops and determination of the centres of origin of the bloodstains, *Forensic Sci. Int.* 6114 (2010) 1–7.
- [17] U. Buck, B. Kneubuehl, Response to 3D bloodstain pattern analysis: ballistic reconstruction of the trajectories of blood drops and determination of the centres of origin of the bloodstains, *Forensic Sci. Int.* 220 (2012) 41.
- [18] M.A. Raymond, E.R. Smith, J. Liesegang, Oscillating blood droplets – implications for crime scene reconstruction, *Sci. Justice* 36 (1996) 161–171.
- [19] R.M. Gardner, Defining the diameter of the smallest parent-stain produced by a drip, *J. Forensic Ident.* 56 (2) (2006) 210–221.
- [20] R. Clift, J.R. Grace, M.E. Weber, Bubbles Drops and Particles, Academic Press, 1978.
- [21] G. Luxford, Experimental and Modelling Investigation of the Deformation, Drag and Break-up of Drizzle Droplets Subjected to Strong Aerodynamic Forces in Relation to SLD Aircraft Icing, (PhD Thesis), Cranfield University, 2005.
- [22] S.A. Krzeczowski, Measurement of liquid droplet disintegration mechanisms, *Int. J. Multiphase Flow* 6 (1980) 227–239.
- [23] L.-P. Hsiang, G.M. Faeth, Drop deformation and breakup due to shock wave and steady disturbances, *Int. J. Multiphase Flow* 21 (1995) 545–560.
- [24] M.C. Jermy, M.C. Taylor, The mechanics of bloodstain pattern formation, in: J. Kieser, M.C. Taylor, D. Carr (Eds.), *Forensic Biomechanics (Developments in Forensic Science)*, Wiley, 2013, pp. 99–136 (Chapter 5) ISBN 9781119990116.
- [25] D. Attinger, C. Moore, A. Donaldson, A. Jafari, H.A. Stone, Fluid dynamics topics in bloodstain pattern analysis: comparative review and research opportunities, *Forensic Sci. Int.* 231 (2013) 375–396.
- [26] A. Wierzb, Deformation breakup of liquid drops in a gas stream at nearly critical Weber numbers, *Exp. Fluids* 9 (1990) 59–64.
- [27] R. Gunn, G.D. Kinzer, The terminal velocity of fall for water droplet in stagnant air, *J. Meteorol.* 54 (1949) 243–248.
- [28] A.W. Green, An approximation for the shape of large raindrops, *J. Clim. Appl. Meteorol.* 14 (1975) 1578–1583.
- [29] P.J. O'Rourke, A.A. Amsden, The TAB Method for Numerical Calculation of Spray Droplet Breakup, SAE Technical Paper 872089, 1987.
- [30] A.B. Liu, D. Mather, R.D. Reitz, Modeling the Effects of Drop Drag and Breakup on Fuel Sprays, SAE Technical Paper 930072, SAE, 1993.
- [31] A. Haider, O. Levenspiel, Drag coefficient and terminal velocity of spherical and nonspherical particles, *Powder Technol.* 58 (1989) 63–70.
- [32] R. Schmehl, Advanced modeling of droplet deformation and breakup for CFD analysis of mixture preparation, in: 18th Annual Conference on Liquid Atomization and Spray Systems, ILASS 2002, 2002, 1–10.
- [33] B.S. Massey, *Mechanics of Fluids*, 6th ed., Chapman Hall, 1989.
- [34] R.D. Reitz, R. Diwakar, Structure of high-pressure fuel sprays, society of automotive engineers technical paper 870598, SAE Trans. 96 (5) (1987) 492–509.
- [35] S. Casson, G. Kurland, Viscometry of human blood for shear rates of 0–100,000 s⁻¹, *Nature* 206 (1965) 617–618.
- [36] G.D.O. Lowe, J.C. Barbenel, in: G.D.O. Lowe (Ed.), *Plasma and Blood Viscosity. Clinical Blood Rheology*, vol. 1, CRC Press, Boca Raton, FL, 1988, pp. 11–44.
- [37] J. Rosina, E. Kvašňák, D. Šuta, H. Kolářová, J. Málek, L. Krajčí, Temperature dependence of blood surface tension, *Physiol. Res.* 56 (1) (2007) S93–S98.
- [38] E. Williams, M.C. Taylor, The development and construction of a motorized blood droplet generation device (BDGD) for detailed analysis of blood droplet dynamics, *J. Bloodstain Pattern Anal.* 29 (1) (2013).
- [39] D. Blair, E. Dufresne, The Matlab Particle Tracking Code Repository, from <http://physics.georgetown.edu/matlab/> (accessed November 2012).
- [40] J.C. Crocker, D. Grier, E.R. Weeks, Particle Tracking Using IDL from <http://www.physics.emory.edu/~weeks/idl/> (accessed November 2012).
- [41] H.R. Pruppacher, R.L. Pitter, A semi-empirical determination of the shape of cloud and rain drops, *J. Atmos. Sci.* 28 (1971) 86–94.
- [42] F.Y. Testik, A.P. Barros, L.F. Bliven, Field observations of multimode raindrop oscillations by high-speed imaging, *Am. Meteorol. Soc.* 63 (2006) 2663–2668.
- [43] S. Chandrasekhar, The oscillations of a viscous liquid globe, *Proc. Lond. Math. Soc.* 9 (1959) 141.
- [44] H. Lamb, *Hydrodynamics*, Cambridge University Press, 1932.
- [45] E. Becker, W.J. Hiller, T.A. Kowalewski, Experimental and theoretical investigation of large amplitude oscillations of liquid droplets, *J. Fluid Mech.* 231 (1991) 189–210.
- [46] J. Tsamopoulos, R.A. Brown, Non-linear oscillations of inviscid drops and bubbles, *J. Fluid Mech.* 127 (1983) 519–537.
- [47] O.A. Basaran, Nonlinear oscillations of viscous liquid drops, *J. Fluid Mech.* 241 (1992) 169.
- [48] L. Rayleigh, On the instability of cylindrical fluid surfaces, *Philos. Mag.* 34 (207) (1892) 177–180.
- [49] E. Brandes, G. Zhang, J. Vivekanandan, Experiments in rainfall estimation with a polarimetric radar in a subtropical environment, *J. Clim. Appl. Meteorol.* 41 (2002) 674–685.
- [50] K.V. Beard, C. Chuang, A new model for the equilibrium shape of raindrops, *J. Atmos. Sci.* 44 (1987) 1509–1524.
- [51] A.C. Best, Empirical formulae for the terminal velocity of water drops falling through the atmosphere, *Quart. J. Meteorol. Soc.* 76 (1950) 302–311.
- [52] E.E. Gossard, R.G. Stauch, D.C. Welsh, S.Y. Matrosov, Cloud layer particle identification, and rain rate profiles from Z, RV measurements by Doppler radars, *J. Atmos. Ocean. Technol.* 9 (1992) 108–119.
- [53] M. Thurai, V.N. Bringi, Drop axis ratios from a 2D-video disdrometer, *J. Atmos. Ocean. Technol.* 22 (2005) 963–975.
- [54] W.G. Umlinger, A new formula for raindrop terminal velocity. Preprints 20th Radar Meteorology Conference, Am. Meteorol. Soc. Boston (1977) 389–391.
- [55] N. Kabaliuk, M.C. Jermy, K. Morison, T. Stotesbury, M.C. Taylor, E. Williams, Blood drop size in passive dripping from weapons, *Forensic Sci. Int.* 228 (2013) 75–82.
- [56] L. Hulse-Smith, M. Illes, A blind trial evaluation of a crime scene methodology for deducting impact velocity and droplet size from circular bloodstains, *J. Forensic Sci.* 52 (1) (2007) 65–69.
- [57] M.J. Sweet, Velocity measurements of projected bloodstains from a medium velocity impact source, *J. Canadian Soc. Forensic Sci.* 26 (3) (1993) 103–110.
- [58] M.C. Taylor, T.L. Laber, B.P. Epstein, D.S. Zamzow, D.P. Baldwin, The effect of firearm muzzle gases on the backscatter of blood, *Int. J. Legal Med.* 125 (5) (2011) 617–628.
- [59] J.H. van Boxel, Numerical model for the fall speed of raindrops in a rainfall simulator, in: Workshop on Wind and Water Erosion, Ghent, Belgium, November 17–18, (1997), pp. 77–85.
- [60] E.E. Michaelides, Particles, Bubbles and Drops – Their Motion, Heat and Mass Transfer, World Scientific Publishers, New Jersey, 2006.
- [61] L. Liang, E.E. Michaelides, The magnitude of Basset forces in unsteady multiphase flow computations, *J. Fluids Eng.* 114 (1992) 417–419.
- [62] N. Kabaliuk, Dynamics of Blood Drop Formation and Flight, (PhD Thesis), University of Canterbury, Christchurch, New Zealand, 2014.
- [63] E.S. Ross, The study of bloodstain patterns resulting from the release of blood drops from a weapon, in Chemistry, The University of Auckland, Auckland, 2006.